16.6 Simulations of a Supercell Thunderstorm with Radiative Transfer, Surface Physics, and a Soil Model

JEFFREY FRAME* AND PAUL MARKOWSKI

Department of Meteorology, Pennsylvania State University, University Park, PA

1. Introduction

Simulations of supercell thunderstorms have traditionally neglected radiative transfer in both the shortwave and longwave regimes. Recent observations, however, suggest that radiative effects can lead to potentially important modifications to the near-storm environment. For example, Markowski et al. (1998) documented surface air temperature deficits of 5–6 K beneath the optically thick anvils of supercell thunderstorms. A pair of numerical simulations of supercell thunderstorms performed by Markowski and Harrington (2005), using an admittedly crude radiative transfer parameterization, found that the inclusion of radiative cooling at the surface beneath clouds, when coupled with a surface sensible heat flux led to large changes in both updraft and mesocyclone strength.

Previous observational studies (e.g., Shabbott and Markowski 2006) have demonstrated the existence of a horizontal buoyancy gradient along the forward-flank outflow boundary of a supercell thunderstorm. It has been shown through numerical simulations (Klemp and Rotunno 1983; Rotunno and Klemp 1985) that the horizontal vorticity generated in this horizontal buoyancy gradient can be tilted into the vertical by the storm's updraft, thereby augmenting the low-level rotation of the mesocyclone. The observations of Markowski et al. (1998) have also revealed horizontal temperature gradients along the edges of anvil shadows, and similar gradients were present in the simulations of Markowski and Harrington (2005). Thus, it is plausible that the horizontal vorticity generated by the temperature gradients along the anvil shadow edges can similarly be tilted into the vertical by the large horizontal gradients in vertical velocity present near the updraft base. It is also possible that the radiative cooling beneath the anvil could decrease the CAPE and increase the CIN within the inflow, leading to a weaker storm.

Herein, we present preliminary results of simulations of supercell thunderstorms that include radiative transfer parameterizations. Three simulations in particular are discussed: two simulations with a detailed radiative transfer parameterization, one of which takes into account the geometry of the direct solar beam; and a simulation with a simple surface radiation budget scheme. Section 2 includes the model details and set-up, section 3 describes the results of the cloud-shading experiments, and the conclusions can be found in section 4.

*Corresponding author address: Jeffrey Frame, Department of Meteorology, Pennsylvania State University, 503 Walker Building, University Park, PA 16802; *e-mail*: jwf155@psu.edu

2. Model description and methodology

The Atmospheric Regional Prediction System (ARPS), version 5.1.5 (Xue et al. 2000, 2001) was employed for all of the simulations. The simulations employed a 150 $\times$ 120 $\times$ 18 km grid, with a horizontal resolution of 1 km and an average vertical resolution of 500 m. The model utilized a stretched vertical coordinate, such that the resolution near the surface was 50 m. A damping sponge layer was prescribed above 13 km.

The model is initialized with an analytic sounding with a small capping inversion, similar to that used by Bluestein and Weisman (2000). The inclusion of a small capping inversion is important because it precludes the widespread development of convection as the low-levels of the model atmosphere are heated via radiation. This thermodynamic profile is depicted in Fig. 1a. Convection is initiated with a warm bubble that has a maximum amplitude of 4 K, a horizontal radius of 10 km, and a vertical radius of 1500 m. This bubble is centered at x = 40 km, y = 30 km, z = 1500 m. The model start time is 21:00 UTC, or 4:00 PM CDT. The initial wind profile consists of a quarter-circle hodograph in the lowest 2 km, followed by pure westerly shear between 2–10 km, such that the low-level storm-relative (s-r) inflow and upper-level s-r outflow make an angle of 30°. The wind speed is constant above 10 km. This hodograph is one that might a priori be expected to lead to significant anvil shading environmental modifications, owing to the slow storm motion and s-r inflow roughly paralleling the major axis of the anvil. The hodograph is shown in Fig. 1b.

Surface fluxes were calculated using simple aerodynamic drag laws. The dimensionless heat and momentum exchange coefficients are 3.0 $\times$ 10^{-3} and the moisture exchange coefficient is 2.1 $\times$ 10^{-3}. The soil model used was from the National Center for Environmental Prediction's Eta model (Pan and Mahrt 1987; Noilhan and Planton 1989; Chen and Dudhia 2001). The soil model consisted of ten vertical layers, with a vertical resolution of 1 cm. Clay soil was used in all three simulations. A six-species cloud microphysics package was used, which included water vapor, rain water, cloud water, cloud ice, snow, and hail/graupel (Lin et al. 1983). The inclusion of surface physics and radiation necessitates the use of zero-gradient boundary conditions on all lateral boundaries; if standard open boundary conditions are used, unrealistic gradients in temperature, moisture, and wind speed develop near the lateral boundaries.

The NASA Goddard Cumulus Ensemble radiative transfer model was used for both shortwave (Chou 1990, 1992; Chou et al. 1998) and longwave (Tao et al. 1996; Chou et al. 1999) radiation. To our knowledge, this and all other radiative transfer models only compute radiative fluxes in the vertical. While

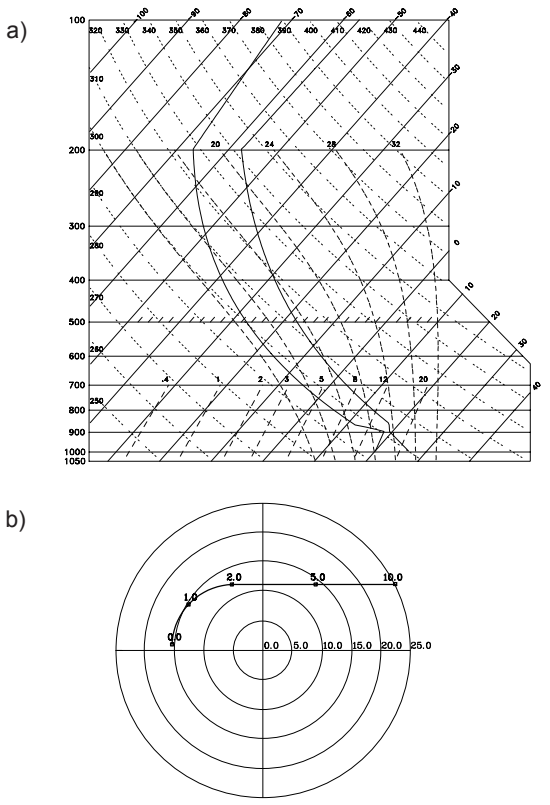

FIG. 1. (a) Skew T-log p diagram depicting the initial temperature and moisture profile. (b) Hodograph depicting the initial wind profile. Winds are in m s^{-1}. Elevations shown at selected points are in km.

this method is acceptable for longwave and diffuse shortwave fluxes, it fails to capture the extention of shadows (due to the shading of the direct beam) when the solar zenith angle is much greater than 0°.

One way to include the angle of the sun in the radiative transfer calculation is to implement a new coordinate system within the radiative transfer model. In this new coordinate system (x', y', z'), the z' axis makes an angle with the true vertical (z) that is equal to the solar zenith angle, θ_s, and x' and y' depend on the solar azimuth angle, ϕ_s. The new coordinate system is used for the direct solar beam only; diffuse solar radiation is still transmitted vertically. A two-dimensional schematic of this coordinate system is provided in Fig. 2.

All grid points at the same vertical level remain on the same horizontal plane, so only a two-dimensional (bilinear) interpolation of the relevent data is required. The data are stored prior to interpolation, so no reinterpolation back the original grid is needed, which may introduce unnecessary error into the model output. If the new vertical axis slants outside of the domain, the data value at the new point is interpolated between the values at the two nearest grid points on the same vertical level. This is consistent with the zero-gradient boundary conditions prescribed in the model.

In three dimensions, the following equations describe the new coordinate system,

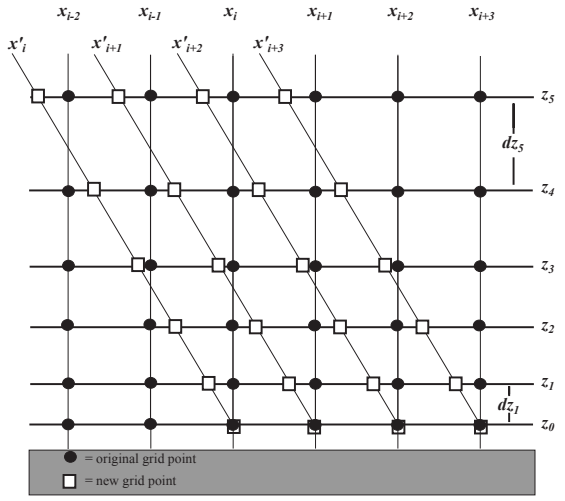

FIG. 2. Schematic depiction of the manner by which a new coordinate system will be defined within the radiative transfer model in order to properly account for the geometry of the cloud shading.

$$x'_i = x_i + \Delta z_k \tan\theta_s \sin\phi_s \tag{1}$$

$$y'_j = y_j + \Delta z_k \tan\theta_s \cos\phi_s \tag{2}$$

$$z'_k = z_k \tag{3}$$

where (x, y, z) are the original model coordinates in the i, j, and k directions, respectively, ϕ_s (the local solar azimuth angle) is taken from the center of the domain and applied everywhere such that the homogeneity of the horizontal grid spacing is maintained (as is the case for θ_s), and

$$\Delta z_k = \sum_{l=1}^{k} dz_l \tag{4}$$

At the conclusion of the solar radiation subroutine, the calculated solar radiation values are interpolated back to the original coordinate system.

This methodology as described above is currently only performed when the solar zenith angle is less than 60°. This prevents interpolation far outside of the model domain, and precludes the possibility of a nearly infinite path length as θ_s approaches 90°. Furthermore, relatively little solar radiation reaches the top of the model atmosphere at these times because the zenith angle is so large. One of the simulations using the detailed radiative transfer package uses this coordinate transformation ("slant"), while the other considers only vertical fluxes of radiation ("no slant").

The simple radiative transfer package used in one of the simulations makes no realistic attempt to account for the reduction of incoming shortwave radiation at the surface due to clouds and water vapor; it is included here as a control simulation. A simulation with the all radiative processes shut off would not be a true control simulation because the radiative scheme continually modifies the ambient environment. The boundary layer in

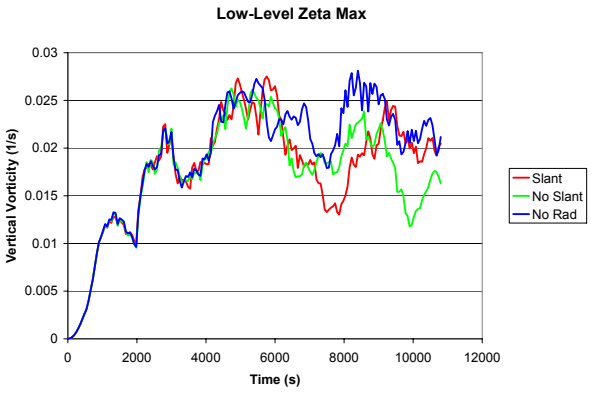

FIG. 3. Time series of the maximum vertical vorticity below 2000 m for all three simulations. "No-Rad" refers to the simulation with a surface radiation budget only.

such a simulation would have a different thermodynamic profile than in a simulation that includes radiation, and a comparison between the two simulations would not be as meaningful. More information on this radiative scheme can be found in Xue et al. (1995).

3. Results

A time series of maximum vertical vorticity (ζ_{max}) below 2000 m (Fig. 3) does not reveal any systematic differences between the simulations. The traces from all three model runs closely match each other through about 4500 s, then diverge after this time. Since the radiative forcing is the only difference between these simulations, these differences must be due to radiatively-driven effects. This is consistent with the results of Markowski and Harrington (2005), who found more similarities than differences over the first hour of their simulations, and divergent results thereafter. Observational evidence also suggests that it takes about an hour for a large, optically thick anvil to develop from the time of initiation of the first towering cumulus. Thus, we restrict the remainder of our analysis to a time when there are significant differences between the simulations, such as 7200 s (2 h).

At 2 h, the net shortwave radiation flux at the surface (Fig. 4) is quite different between the simulations. In the simulation with the full shading geometry, there is a large surface area receiving less than 50 W m^{-2} of shortwave radiation that extends nearly 30 km downwind of the precipitation core (Fig. 4a). This region only goes about 15 km downwind in the no-slant simulation, but is wider in the meridional direction (Fig. 4b). This extra meridional width may be attributable to a broader precipitation region in the no-slant simulation. Additionally, the radiative flux field is smoother in the no-slant simulation because clouds tend to grow vertically, not at an angle to the vertical. The surface shortwave radiation flux in the simulation with the surface radiation budget only ("no rad") is between 400–450 W m^{-2} everywhere.

It is well-known that radiatively-forced temperature changes in the boundary layer are driven by the heating and cooling of the earth's surface (e.g., the mean diurnal temperature cycle). Thus, the radiative flux data presented above would likely have a large influence on the skin temperature, or the temperature of the top layer of the soil model. In the slant simulation, the expanse of sub-300 K skin temperatures extends over 40 km downstream from the precipitation core (Fig. 5a), and only about 15–20 km downstream in the no-slant simulation (Fig. 5b). The skin temperature fields closely match the anvil shadow seen in the radiation flux fields above. Also, there is no

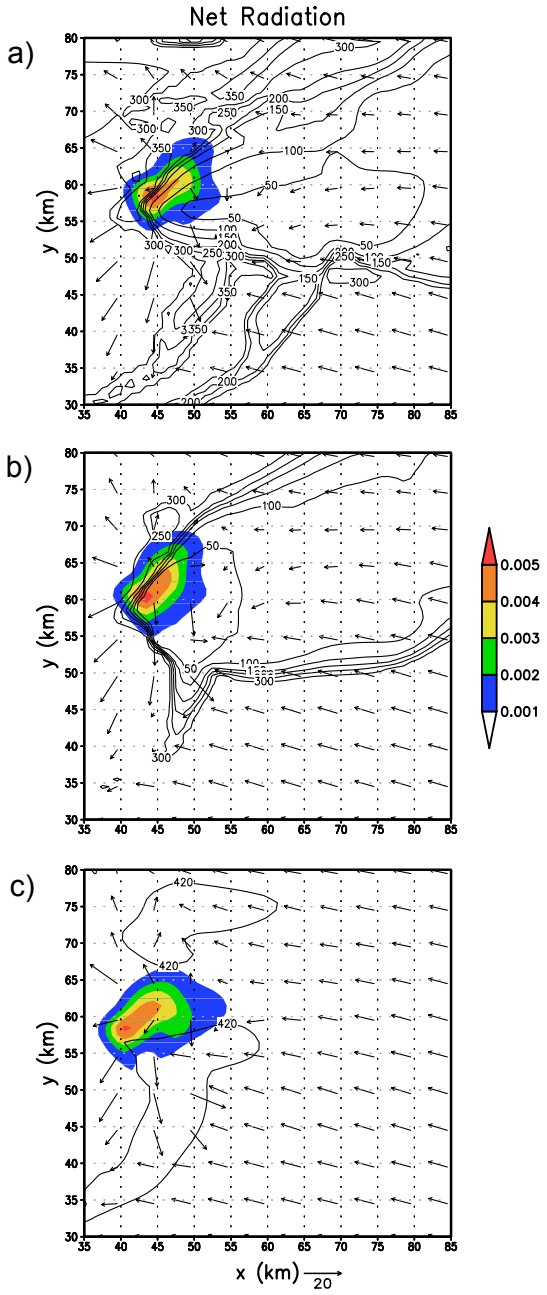

FIG. 4. Surface shortwave radiation flux (contoured) and rainwater mixing ratio (shaded) at 7200 s for (a) the slant simulation, (b) the no-slant simulation, and (c) the surface radiation budget only simulation. Wind vectors at 25 m are also plotted and scaled as indicated. Contour interval is 50 W m^{-2}.

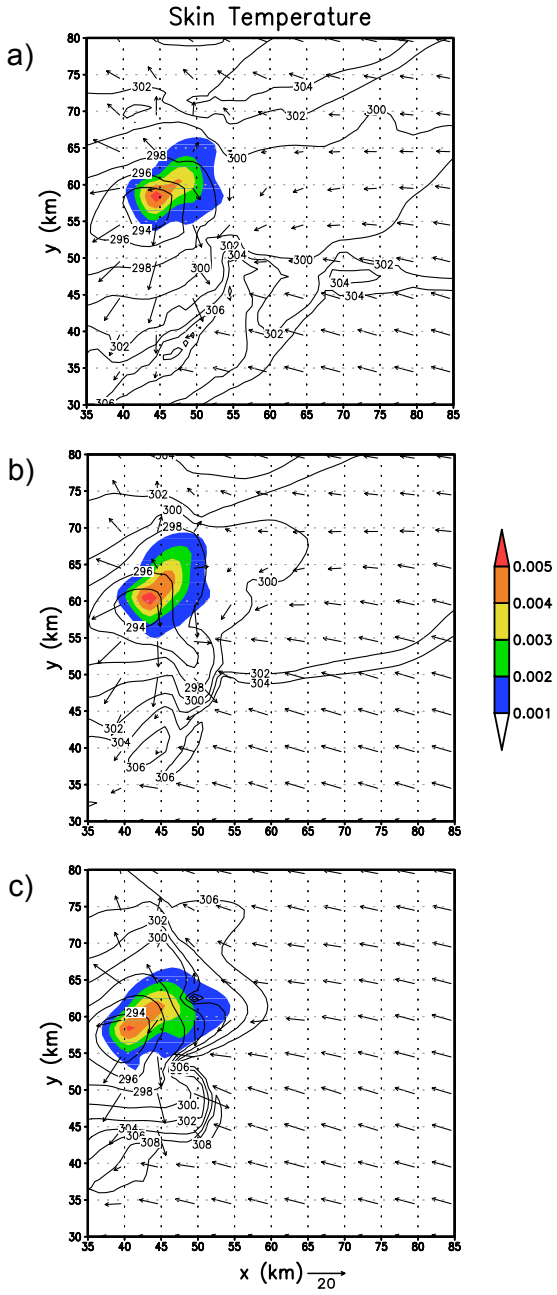

FIG. 5. Skin temperature (contoured) and rainwater mixing ratio (shaded) at 7200 s for (a) the slant simulation, (b) the no-slant simulation, and (c) the surface radiation budget only simulation. Wind vectors at 25 m are also plotted and scaled as indicated. Contour interval is 2 K.

shaded area of cooler skin temperatures downstream from the storm in the run with the surface radiative budget only (Fig. 5c), meaning that this cooling seen in the other two simulations is entirely caused by the anvil shadow. The largest skin temperature deficits in all of the simulations is within the region of heavy precipitation, where evaporatively cooled air has chilled the surface.

Not surprisingly, the air temperature at the lowest model level (z = 25 m) is also reduced in the areas of strong radiative cooling at the surface (Fig. 6). Air temperature deficits up to 1.5–2.0 K are seen outside of the forward-flank outflow in the slant simulation (Fig. 6a). These deficits are generally 25–50% smaller in the no-slant simulation (Fig. 6b), and are absent in the simulation without cloud-shading effects (Fig. 6c). The greatest expanse of cool air beneath the anvil is in the slant simulation, which is consistent with the more expansive area of radiative cooling in that simulation. This anvil shading leads to the development of a temperature gradient along the southern border of the anvil cloud in the slant simulation (Fig. 6a). This feature is also present in the no-slant simulation, but is significantly weaker (Fig. 6b) due to less radiative cooling in that simulation.

One hypothesis set forth in the Introduction is that the temperature gradients produced along anvil edges could serve as an important source of horizontal vorticity to be tilted by the updraft. The low-level winds along this gradient suggest that any horizontal vorticity produced within this gradient would be almost purely streamwise. The time series of ζ_{max} (Fig. 3), however, illustrates that even if this is occurring, it is likely being offset by some other effect, such as an increase in CIN beneath the anvil. This is a subject of future investigation. In fact, the slant simulation rarely has the largest values of low-level ζ_{max} at any time after 6000 s.

Horizontal cross sections of 1000 m vertical velocity and 200 m vertical vorticity (Fig. 7) illustrate that the slant simulation, which has the strongest radiative cooling, has weaker low-level rotation and updrafts than the other two simulations. The simulation without anvil shading has the strongest vertical motions along the rear-flank gust front owing to a greater density difference across the boundary, owing to the presence of warmer air beneath the anvil.

Furthermore, the forward-flank temperature gradient is much stronger in the simulation without cloud shading because relatively warmer inflow is able to make it much closer to the storm (Fig. 6c). There is also a signature of the forward-flank temperature gradient in the no-slant simulation southeast of the main precipitation core (Fig. 6b), but such a feature is weak and diffuse in the slant simulation (Fig. 6a). Thus, it appears that the stronger forward-flank temperature gradient is more beneficial to the storm than the radiatively-generated temperature gradient in the slant simulation. It also seems likely that, at least for this set of environmental conditions, the large mass of radiatively cooled air beneath the anvil is more detrimental to the storm than any temperature gradient along the edge of the anvil is beneficial to it.

Also, it is worth noting that the prior emphasis on the forward-flank region of the storm based on the simulations of Klemp and Rotunno (1983) and Rotunno and Klemp (1985) is perhaps overdone. Observations have shown (e.g., Shabbott and Markowski 2006) that forward-flank temperature gradients are often not as strong as in these modelling studies, and these differences could be because radiation was neglected in these simulations.

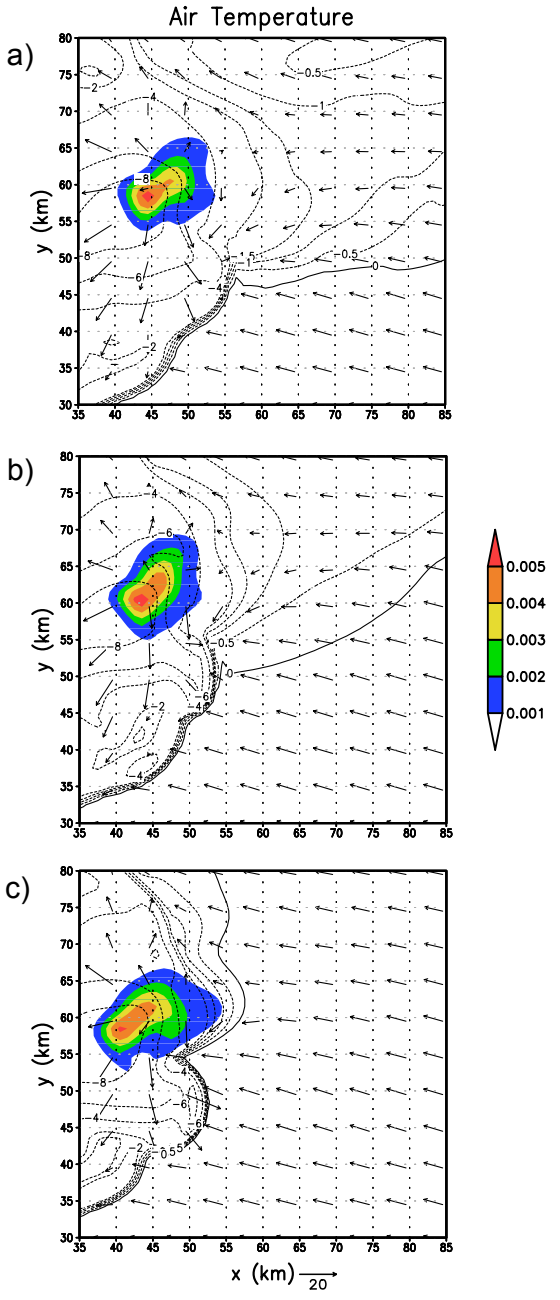

FIG. 6. Air temperature deficit at 25 m (contoured) and rainwater mixing ratio (shaded) at 7200 s for (a) the slant simulation, (b) the no-slant simulation, and (c) the surface radiation budget only simulation. Wind vectors at 25 m are also plotted and scaled as indicated. Irregular contours are 0, –0.5, –1.0, –1.5, –2.0, –4.0 and –8.0 K.

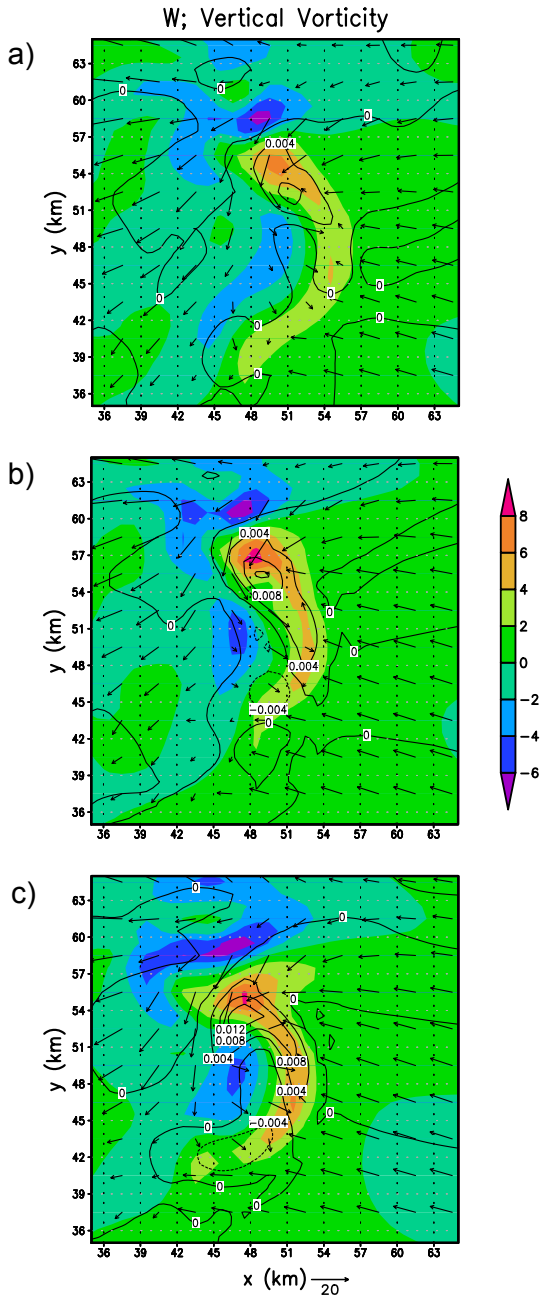

FIG. 7. Vertical vorticity at 200 m (contoured) and vertical velocity at 1000 m (shaded) at 7200 s for (a) the slant simulation, (b) the no slant simulation, and (c) the surface radiation budget only simulation. Wind vectors at 200 m are also plotted and scaled as indicated. Contour interval is 0.004 s^{-1}.

4. Conclusions

The set of simulations presented herein illustrate that the inclusion of radiative transfer parameterizations, traditionally neglected in simulations of supercell thunderstorms, can influence both the storm and the near-storm environment. The shading beneath the anvil cloud leads to a large area with temperature deficits of 1–2 K, which leads to a weaker updraft, low-level rotation, and forward-flank gust front. The temperature gradients produced along the anvil edges are shown to be of less importance.

These simulations also show that the current method of computing only vertical fluxes of the direct solar beam within radiative transfer models is insufficient to capture all storm-scale radiative processes. The coordinate transformation proposed herein produces physically realistic results at minimal compu-

tational cost.

We emphasize that the results presented herein are only the beginning of a much larger study. Many more wind profiles will be tested because the residence time of inflow within radiatively-generated temperature gradients or temperature deficits should dictate the relative importance of these effects. The features examined above are Galilean invariant, meaning that the ground-relative, not storm-relative, wind profile is important. Thus, we hope to investigate storms that are fast-moving, in addition to the slow-moving storms seen in this paper. Also, preliminary tests reveal that stronger anvil-shading effects develop if the model is initialized at an earlier time, when the sun is higher in the sky. We also seek to utilize different land surface types, as other preliminary tests have shown an alarming sensitivity to the land surface used. Finally, we also hope to extend this study to non-supercellular convection, such as multicells and pulse storms.

Acknowledgments. We wish to thank Dave Stauffer for allowing us to use his computing cluster. We also had many insightful discussions with Yvette Richardson and Rob Carver that improved this work. ARPS is a product of the Center for Analysis and Prediction of Storms at the University of Oklahoma. All cross-sectional figures shown were produced using GrADS software. Support from NSF grant ATM-0338661 also is acknowledged.

REFERENCES

Bluestein, H. B. and M. L. Weisman, 2000: The interaction of numerically simulated supercells initiated along lines. *Mon. Wea. Rev.*, **128**, 3128–3149.

Chen, F. and J. Dudhia, 2001: Coupling an advanced land surface-hydrology model with the Penn State-NCAR MM5 modeling system. Part I: Model implementation and sensitivity. *Mon. Wea. Rev.*, **129**, 569–585.

Chou, M.-D., 1990: Parameterizations for the absorption of solar radiation by O_2 and CO_2 with application to climate studies. *J. Climate*, **3**, 209–217.

Chou, M.-D., 1992: A solar radiation model for use in climate studies. *J. Atmos. Sci.*, **49**, 762–772.

Chou, M.-D., M. J. Suarez, C.-H. Ho, M. M.-H. Yan and K.-T. Lee, 1998: Parameterizations for cloud overlapping and shortwave single-scattering properties for use in general circulation and cloud ensemble models. *J. Climate*, **11**, 202–214.

Chou, M.-D., K.-T. Lee, S.-C. Tsay, and Q. Fu, 1999: Parameterization for cloud longwave scattering for use in atmospheric models. *J. Climate*, **12**, 159–169.

Klemp, J. B. and R. Rotunno, 1983: A study of the tornadic region within a supercell thunderstorm. *J. Atmos. Sci.*, **40**, 359–377.

Lin, Y.-L., R. D. Farley, and H. D. Orville, 1983: Bulk parameterization of the snow field in a cloud model. *J. Appl. Meteor.*, **22**, 1065–1092.

Markowski, P. M. and J. Y. Harrington, 2005: A simulation of a supercell thunderstorm with emulated radiative cooling beneath the anvil. *J. Atmos. Sci.*, **62**, 2607–2617.

Markowski, P. M., E. N. Rasmussen, J. M. Straka, and D. C. Dowell, 1998: Observations of low-level baroclinity generated by anvil shadows. *Mon. Wea. Rev.*, **126**, 2942–2958.

Noilhan, J. and S. Planton, 1989: A simple parameterization of land surface processes for meteorological models. *Mon. Wea. Rev.*, **117**, 536–549.

Pan, H.-L. and L. Mahrt, 1987: Interaction between soil hydrology and boundary-layer development. *Bound.-Layer Meteor.*, **38**, 185–202.

Rotunno, R. and J. B. Klemp, 1985: On the rotation and propagation of simulated supercell thunderstorms. *J. Atmos. Sci.*, **42**, 271–292.

Shabbott, C. J., and P. M. Markowski, 2006: Surface in situ observations within the outflow of forward-flank downdrafts of supercell thunderstorms. *Mon. Wea. Rev.*, **134**, 1422–1441.

Tao, W.-K., S. Lang, J. Simpson, C.-H. Sui, B. Ferrier, and M.-D. Chou, 1996: Mechanisms of cloud-radiation interaction in the Tropics and Midlatitudes. *J.Atmos. Sci.*, **53**, 2624–2651.

Xue, M., K. K. Droegemeier, V. Wong, A. Shapiro, and K. Brewster, 1995: *ARPS 4.0 User's Guide.* Center for Analysis and Prediction of Storms, University of Oklahoma, 380 pp.

Xue, M., K. K. Droegemeier and V. Wong, 2000: The Advanced Regional Prediction System (ARPS): A multiscale nonhydrostatic atmospheric simulation and prediction tool. Part I: Model dynamics and verification. *Meteor. Atmos. Phys.*, **75**, 161–193.

Xue, M., K. K. Droegemeier, V. Wong, A. Shapiro, K. Brewster, F. Carr, D. Weber, Y. Liu and D. H. Wang, 2001: The Advanced Regional Prediction System (ARPS): A multiscale nonhydrostatic atmospheric simulation and prediction tool. Part II: Model physics and applications. *Meteor. Atmos. Phys.*, **76**, 143–165.